Electronic Journal of Biotechnology 78 (2025) 14–25

Contents lists available at ScienceDirect

Electronic Journal of Biotechnology

journal homepage: www.elsevier.com/locate/ejbt

Research article

Tianma granules: Bridging traditional medicine and modern science to combat colorectal cancer via ferroptosis ☆

Ning Ding [a,b], Xiaojuan Tang [a], Yijing Zhang [c], Hongbiao Luo [c,d], Yanbo Tang [a], Chaoqun Zeng [c], Yongheng He [a,*], Liang Zhao [a,*]

[a] Department of Anorectal Surgery, The Affiliated Hospital of Hunan Academy of Traditional Chinese Medicine, Changsha, Hunan, PR China
[b] Institute of Life and Medical Sciences, Hunan University, Changsha, Hunan, PR China
[c] Graduate School, Hunan University of Chinese Medicine, Changsha, Hunan, PR China
[d] Department of Anorectal Surgery, Chenzhou No. 1 People's Hospital, Chenzhou, Hunan, China

GRAPHICAL ABSTRACT

Tianma granules: Bridging traditional medicine and modern science to combat colorectal cancer via ferroptosis.

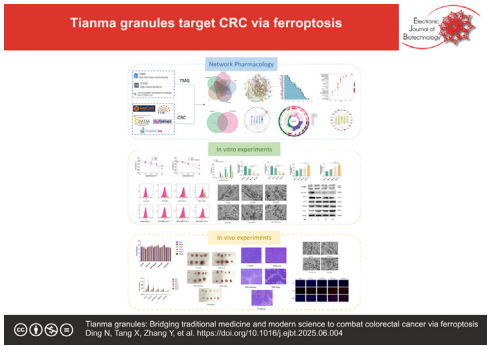

ARTICLE INFO

Article history:
Received 7 March 2025
Accepted 2 June 2025
Available online 23 August 2025

Keywords:
Anti-cancer potential
Colorectal cancer
Experimental verification
Ferroptosis
Mitochondrial fragmentation
Mitochondrial vacuolation
Network pharmacology
Therapeutic target
Tianma granules

ABSTRACT

Background: This study aims to investigate the ferroptosis-inducing effects of Tianma Granules (TMGs) in colorectal cancer and elucidate its molecular mechanisms. Ferroptosis, an iron-dependent form of regulated cell death, represents a novel therapeutic target for cancer. We combined network pharmacology with experimental validation to explore TMG's anti-cancer potential through ferroptosis modulation.
Results: Network pharmacology identified 382 ferroptosis-related genes overlapping with 12,944 CRC-associated targets ($p < 0.05$), with SLC7A11, GPX4, SAT1, PTGS2, and GLS2 prioritized as core targets. *In vitro*, TMG dose-dependently suppressed CRC cell proliferation ($p < 0.05$), elevated reactive oxygen species ($p < 0.05$) and ferrous ion levels ($p < 0.01$), effects reversed by ferroptosis inhibitor, Ferrostatin-1. c-Casp3 levels were unchanged ($p > 0.05$), excluding apoptosis. Transmission electron microscopy revealed mitochondrial cristae fragmentation and vacuolation, hallmark features of ferroptosis. Molecular analyses demonstrated TMG-mediated downregulation of SLC7A11 and GPX4, alongside upregulation of SAT1, PTGS2, and GLS2 ($p < 0.05$). In xenograft models, high-dose TMG (23.2 g/kg) reduced tumor volume, attenuated cachexia, and elevated intratumoral ROS and Fe^{2+} levels ($p < 0.01$), corroborating ferroptosis induction *in vivo*.

☆ Audio abstract available in Supplementary material.

Peer review under responsibility of Pontificia Universidad Católica de Valparaíso.

* Corresponding authors.
E-mail addresses: 2320990685@qq.com (Y. He), heather999@163.com (L. Zhao).

https://doi.org/10.1016/j.ejbt.2025.06.004

Conclusions: TMG suppresses CRC progression by inducing ferroptosis via dual inhibition of SLC7A11/GPX4 and activation of SAT1/PTGS2/GLS2. This study bridges traditional medicine and ferroptosis biology, positioning TMG as a novel therapeutic candidate for CRC.

How to cite: Ding N, Tang X, Zhang Y, et al. Tianma granules: Bridging traditional medicine and modern science to combat colorectal cancer via ferroptosis. Electron J Biotechnol 2025;78. https://doi.org/10.1016/j.ejbt.2025.06.004.

1. Introduction

Colorectal cancer (CRC) remains a leading contributor to cancer-related morbidity and mortality worldwide, highlighting the imperative for novel therapeutic strategies to improve patient outcomes [1]. Current treatment options, including chemotherapy and targeted therapies, often face challenges such as drug resistance and adverse side effects, thereby emphasizing the urgent need for alternative treatment approaches [2]. Recent research has elucidated several molecular pathways and genetic alterations that drive CRC progression, particularly the activation of oncogenic signaling pathways and the disruption of tumor suppressor gene functions [3]. However, despite significant advancements in understanding CRC pathophysiology, there is a notable gap in the exploration of traditional medicinal therapies and their potential roles in CRC management.

The patented formulation of Tianma Granules is utilized in the treatment of colorectal cancer and comprises several critical components: centipede and scorpion, which are employed for their toxin-counteracting properties; seaweed and Nanxing, which facilitate the transformation of phlegm and the softening of hard masses; Huangbo and Banbianlian, which are used for their heat-clearing and detoxifying effects; Sanleng and Dahuang, which promote blood circulation and resolve stasis; and Huangqi and Shanyao, which are included for their Qi tonifying and spleen-strengthening capabilities. This formulation is designed to eradicate pathogens while preserving the body's vital energy and to bloster the body's defenses against the recurrence of pathogens. Empirical research suggests that Tianma Granules can enhance the quality of life and extend survival in patients with advanced colorectal cancer, inhibit postoperative recurrence, and mitigate toxic side effects [4,5,6,7]. Despite its notable clinical efficacy, current research is predominantly confined to single targets and pathways; thus, a more comprehensive understanding of the intricate mechanisms underlying this compound is imperative. The integrated strategy combining network pharmacology and experimental validation, as outlined in Fig. 1, systematically explores TMG's multi-target mechanisms against CRC through ferroptosis modulation.

The integration of network pharmacology with experimental validation presents a promising approach for elucidating the mechanisms through which TMG may contribute to CRC treatment. Network pharmacology utilizes a systems biology approach to elucidate the intricate interactions between pharmacological agents and biological systems, thereby providing insights into the molecular networks that underpin drug actions [8,9,10]. By integrating bioinformatics analyses with empirical data, researchers can identify key gene targets and signaling pathways modulated by TMG, offering a comprehensive understanding of its therapeutic potential in CRC.

Ferroptosis, a regulated form of cell death characterized by iron-dependent lipid peroxidation, has recently emerged as a significant factor in cancer biology [11]. Dysregulation of ferroptosis-related pathways has been associated with tumorigenesis and cancer progression, making it an attractive target for therapeutic interventions. Preliminary findings indicate that TMG may induce ferroptosis in CRC cells by modulating the expression of crucial genes involved in this mechanism, including SLC7A11 and GPX4. These observations highlight the need for an in-depth investigation into the manner in which TMG affects ferroptosis and the subsequent ramifications for CRC treatment.

This study aims to systematically examine the impact of TMG on the proliferation of CRC cells and to elucidate the molecular mechanisms at play, with a specific focus on the expression of genes associated with ferroptosis and their related pathways.

2. Materials and methods

2.1. Study design and workflow

The three-phase experimental framework comprises: Target Screening Phase: Integrated network pharmacology analysis of CRC and ferroptosis targets from TCGA, OMIM, etc. In Vitro Validation: CRISPR-based screening of ferroptosis markers (ROS, Fe^{2+}, mitochondrial). In Vivo Evaluation: Subcutaneous xenograft model establishment for assessing TMG's antitumor efficacy.

2.2. Network pharmacology

2.2.1. Identification of colorectal cancer targets and ferroptosis

Related Genes: Relevant genes associated with "colorectal cancer" were identified using the following five databases: GeneCards (https://www.genecards.org/), OMIM (https://www.omim.org/), PharmGKB (https://www.pharmgkb.org/), TTD (https://db.idrblab.net/ttd/), and DisGeNET (https://www.disgenet.org/). GeneCards Database targets retaining 'Experimental evidence' tags (including 'Biochemical assay', 'RNAi', 'CRISPR', and 'Antibody' validation levels) were prioritized. All predictions exclusively relying on text mining or homology analyses were discarded. The Venn package in R was employed to determine the common genes identified across these databases. For genes related to ferroptosis, the FerrDb database (https://www.zhounan.org/ferrdb/current/) was consulted. Subsequently, the Venn package was utilized again to find the intersection between the colorectal cancer-related targets and ferroptosis-associated genes.

2.2.2. Screening of active ingredients and targets of Tianma granules

The eight herbal constituents of Tianma granules, namely "Huangbai" (Phellodendron), "Sanleng" (Rhizoma Sparganii), "Dan Nanxing" (Arisaema), "Haizao" (Sargassum), "Huangqi" (Astragalus), "Shanyao" (Chinese Yam), and "Shu Dahuang" (Processed Rhubarb), were meticulously selected. The selection criteria included oral bioavailability (OB) $\geq$ 30% and drug likeness (DL) $\geq$ 0.18. The identification of effective active components and their targets is conducted utilizing the Traditional Chinese Medicine Systems Pharmacology Database and Analysis Platform (TCMSP) (https://old.tcmsp-e.com/tcmsp.php) [12].

For the animal-derived medicines "Scorpion" (Scorpio) and "Centipede" (Scolopendra), an exhaustive search is performed

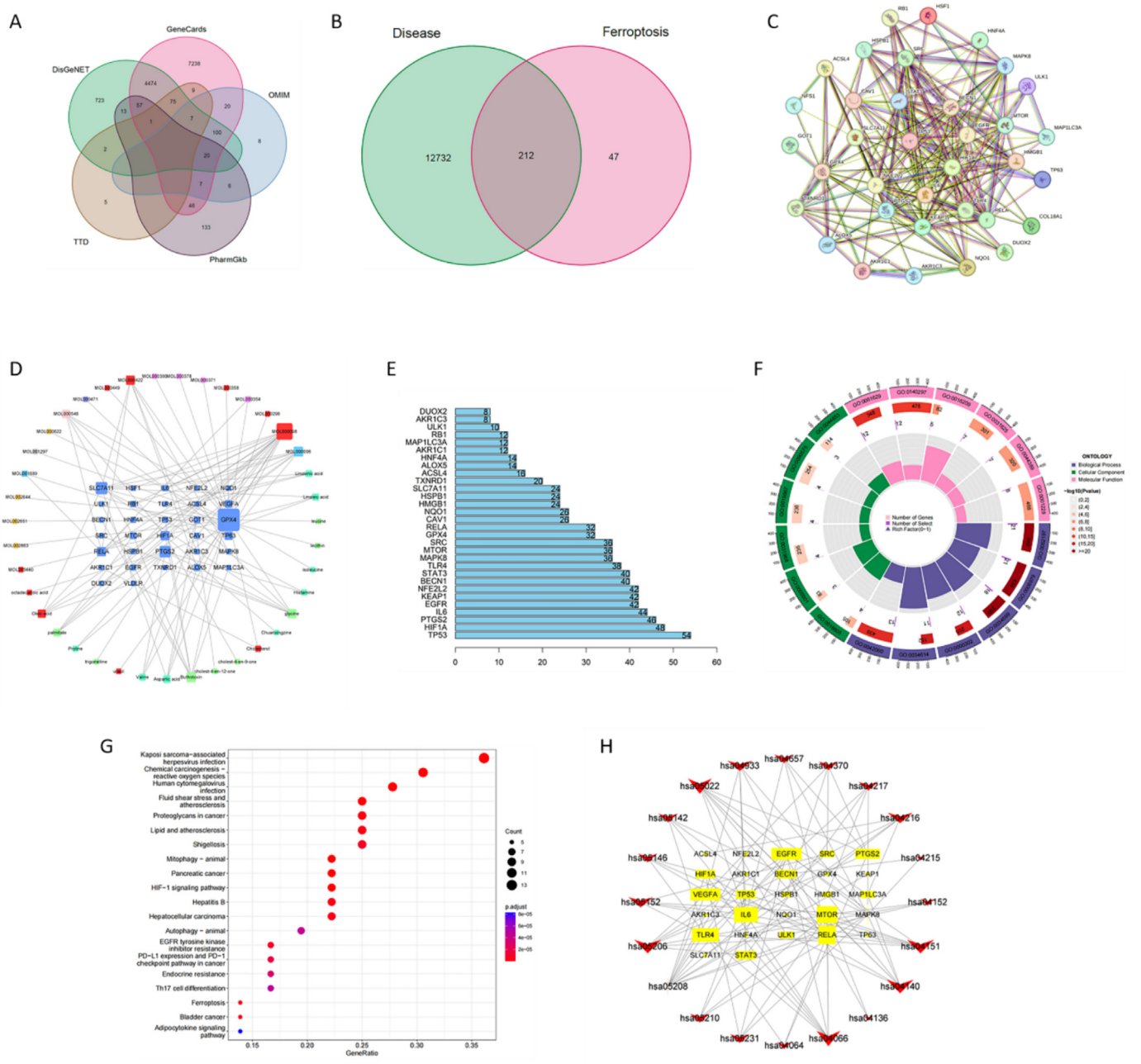

Fig. 1. Network pharmacology and functional enrichment analysis of Tianma granules (TMGs) in colorectal cancer ferroptosis regulation. (A) Venn diagram showing CRC-associated targets from five databases (GeneCards, OMIM, PharmGKB, TTD, DisGeNET). (B) Intersection of 382 ferroptosis genes (FerrDb) with CRC targets. (C) PPI network of TMG-CRC-ferroptosis targets, highlighting top hub genes (PTGS2, GPX4, SLC7A11). (D) TMG-CRC-ferroptosis regulatory network with color-coded nodes: herbal components (purple), genes (blue), and shared targets (red). (E) Top 30 hub targets ranked by node connectivity. (F) GO enrichment: oxidative stress (biological processes), mitochondrial membranes (cellular components), transcription factor binding (molecular functions). (G) KEGG pathway enrichment: bubble size = gene count; color = adjusted p – value. (H) KEGG pathway-target network: red nodes = pathways, yellow nodes = targets. (For interpretation of the references to color in this figure legend, the reader is referred to the web version of this article.)

across databases such as CNKI, Wanfang, Weipu, the China Biomedical Literature Database, and PubMed to compile all relevant chemical constituents [13,14,15]. The previously acquired chemical components are then explored in the TCMSP database, the Traditional Chinese Medicine Integrated Pharmacology Research Platform (TCMIP), and the Comparative Toxicogenomics Database (CTD) (https://ctdbase.org/) [16] to document the corresponding target proteins or genes for each component. Finally, a computational script is utilized to integrate the chemical constituents with their respective target proteins.

2.2.3. Network diagram of potential target genes in TMG-CRC-Ferroptosis

The Venn package was utilized to identify the intersection of CRC and ferroptosis-related targets with the target genes of Tianma granules, thereby identifying co-expressed targets linked to diseases, phenotypes, and pharmaceuticals. Furthermore, a Perl script and Cytoscape 3.8.2 software [17] (available at https://www.cytoscape.org/) were employed to integrate the active components and construct the target co-expression network diagram for Tianma granules in the management of colorectal cancer. Within

the network, circular nodes of various colors represent distinct drugs and target genes or proteins, while the connecting lines illustrate the relationships between compounds and co-expressed targets.

2.2.4. Protein-Protein Interaction Networks (PPI) and potential target screening

The STING database [18] (https://cn.string-db.org/) was used to analyze protein–protein interactions of co-expressed targets related to CRC, ferroptosis, and Tianma granules. Networks were generated with high-confidence edges (interaction score >0.7), and interactions supported merely by co-expression or database co-occurrence evidence were eliminated. The species information was set to human, and unconnected nodes were excluded. The resulting protein interaction network will be analyzed using R language to determine the expression levels of key target proteins, based on node connectivity.

2.2.5. Gene Ontology (GO) Function and Kyoto Encyclopedia of Genes and Genomes (KEGG) pathway enrichment analysis

The org.hs.eg package will be utilized to convert target IDs. Subsequently, GO and KEGG pathway enrichment analyses will be conducted using the cluster Profiler, DOSE, and enrichment plot packages, with a significance threshold set at $p < 0.05$. The GO enrichment results, encompassing biological processes (BPs), cellular components (CCs), and molecular functions (MFs), will be illustrated through bar charts. The KEGG pathway enrichment results will be depicted using bubble plots. Additionally, Cytoscape will be employed to visualize the KEGG enrichment network, where node size indicates varying levels of enrichment and the connections between nodes represent the relationships between targets and pathways.

2.3. Cell culture

Human colorectal cancer cell lines SW620 and HT29 were procured from the Shanghai Cell Bank of the Chinese Academy of Sciences. Both SW620 and HT29 cells were cultured in DMEM medium (11995-065, Gibco, New York, USA), supplemented with 10% fetal bovine serum (10099-141, Gibco, New York, USA) and appropriate antibiotics (15140122, Gibco, New York, USA). Cultivation was conducted at 37°C in a 5% CO_2 environment, with regular monitoring of cell growth status. All experiments were performed with ≥3 independent biological replicates (n = 3 batches of cell cultures).

2.4. Laboratory animals

The experimental subjects comprised 40 SPF-grade male SD rats (6 weeks old, weighing 180–220 g), acquired from Hunan Slyke (License No. SYXK (Xiang) 2019–0009), adhering to animal welfare and ethical standards, and sanctioned by Hunan University of Chinese Medicine. TMG dosing (5.8–23.2 g/kg) followed human-to-rat body surface area conversion [19] (10 g/60 kg human → 5.8 g/kg rat equivalent) [20], with high dose validated as non-toxic in preliminary studies (LD50 > 50 g/kg). The rats were housed under a 12-h light–dark cycle, with the ambient temperature controlled between 20 and 24°C and humidity maintained at 42–55%. The facility ensured adequate ventilation and cleanliness, and the animals were provided with unrestricted access to food and water.

In addition to the SD rats, the investigation also included 25 SPF-grade male BALB/c nude mice and 25 female BALB/c nude mice, each 4 weeks old and weighing 18–20 g. These mice were similarly obtained from Hunan Slyke (License No. SYXK (Xiang) 2019-0004), and the SPF-grade animal quality certification (**Fig. S1**) and institutional ethics approval license (**Fig. S2**) are provided as supporting documentation. They were housed under conditions equivalent to those of the SD rats. The care and use of these animals adhered to the same ethical guidelines and were sanctioned by the Hunan University of Chinese Medicine.

2.5. Preparation of herbal extracts

The Tianma granules utilized in this study were procured from the Affiliated Hospital of Hunan Academy of Traditional Chinese Medicine. These granules were produced by the hospital's Pharmacy Department, received approval from the Hunan Provincial Food and Drug Administration, and successfully passed quality inspections. Each packet of Tianma granules contains 10 g, with the recommended adult dosage being one packet twice daily. The granules were dissolved in water, filtered multiple times, concentrated to a solution with a concentration of 0.175 g/ml, sterilized, sealed, and stored at a temperature of 4°C.

2.6. Preparation of blank serum and drug-containing serum

SPF-grade SD male rats were divided into two groups: one receiving drug-treated serum and the other receiving normal serum. The rats in the drug-treated group were administered Tianma granules at a dosage equivalent to that recommended for a 70 kg adult. The Tianma solution, with a concentration of 0.175 g/ml, was administered at a rate of 10 ml/kg twice daily for 6 d. Following this period, the rats underwent fasting and water deprivation. On the 7th d, the rats were anesthetized, and blood samples were collected. The blood was subsequently centrifuged, and the serum was inactivated at 56°C, filtered, and stored at −80°C.

2.7. Construction of subcutaneous xenograft model construction

Acquire 4-week-old BALB/c nude mice, comprising both male and female specimens, each weighing between 18 and 20 g. Randomly allocate the mice into groups of ten, ensuring each group consists of an equal number of males and females. Assign ear tags for identification purposes. During the logarithmic growth phase, collect SW620 cells, subject them to trypsin digestion, and centrifuge to eliminate the supernatant and to resuspend the cell pellet in PBS, adjusting the cell density to 1×10^7 cells/ml. Sterilize the skin on the left flank of each nude mouse with alcohol. Using a 1 mL syringe, aspirate the cell suspension. Following disinfection of the injection site, administer approximately 0.1 mL of the cell suspension subcutaneously to a depth of approximately 1 cm. Post-injection, apply gentle pressure to the site with tweezers and observe for the development of tumor cell masses.

2.8. Administration and body weight

Monitoring in Nude Mice: Organize the nude mice into distinct groups: model, low-dose Tianma granule, medium-dose Tianma granule, high-dose Tianma granule, and oxaliplatin. Dosage calculations for the mice are derived from human body surface area conversion. The model group will receive 0.9% normal saline at a dosage of 20 mL/kg, while the Tianma granule groups will be administered daily doses of 5.8 g/kg, 11.6 g/kg, and 23.2 g/kg for 16 d. The oxaliplatin treatment group is scheduled to receive an injection of 8 mg/kg on specified days. Tumor dimensions are recorded with the long diameter designated as "a" and the short diameter as "b". Tumor volume is calculated using the formula ($V = a \times b^2 \times 0.5$).

2.9. Specimen collection and hematoxylin and eosin (HE)

Tumor specimens are collected, rinsed with saline, and fixed in 10% formalin for a duration of 24 h. Following fixation, the specimens undergo dehydration through a graded ethanol series. The slides are dewaxed in xylene treated with heavy water, and rinsed before undergoing hematoxylin and eosin staining. The slides are then dehydrated, cleared mounted, and examined microscopically.

2.10. CCK8 verifies assessment via CCK8 assay

SW620 and HT29 cells are seeded at a density of 5×10^4 cells per well in a 96-well plate, with each experimental group having three replicates. After an overnight incubation period, drug treatments are administered at 0, 24, and 48 h. Subsequently, 10 μL of CCK8 solution (CCK8, A311-02, Vazyme, Nanjing, China) is added, and the plates are incubated at 37°C in a 5% CO_2 atmosphere for 4 h. Absorbance is measured at 450 nm to assess cell viability.

2.11. Reactive oxygen species (ROS) measurement for flow cytometry

SW620 cells are resuspended to achieve a concentration of 50,000 to 100,000 cells per mL. Add 195 μL of Annexin V-FITC binding solution (Annexin V-FITC, C1062S, Beyotime, Shanghai, China) and mix thoroughly. Subsequently, introduce 5 μL of Annexin V-FITC and 10 μL of propidium iodide (PI). Incubate the mixture in darkness for 20 min, followed by fluorescence measurement using a flow cytometer. For SW620 cells at 60–70% confluence, administer serum containing the drug along with 10 μM ferrostatin-1. Incubate at 37°C in a 5% CO_2 atmosphere for 24 h. Following the removal of the medium, dilute DCFH-DA in serum-free DMEM (1:1000) and incubate for 30 min prior to assessing ROS levels (S0033M, Beyotime, Shanghai, China).

2.12. Measurement of Fe^{2+} levels

The quantification of ferrous ions (Fe^{2+}) was conducted using the Elabscience colorimetric assay kit (E-BC-K773-M, Elabscience, Wuhan, China), a reliable tool for such evaluations. After a specified incubation period, 300 μL of the resultant supernatant was carefully transferred to a 96-well plate designated for optical measurements. The optical density (OD) was then measured at a wavelength of 593 nm using a microplate reader, enabling the precise quantification of the Fe^{2+} concentration in the sample.

2.13. TEM to observe for cellular morphological analysis

Following initial fixation, SW620 cells underwent enzymatic digestion and were subsequently fixed in 2.5% glutaraldehyde for a duration of 6 h. This was followed by secondary fixation with 1% osmium tetroxide at 4°C for 90 min. The cells were subjected to a graded dehydration process utilizing ethanol and acetone, with each step lasting 15 min. The samples were then embedded in a resin mixture overnight and polymerized at 60°C over a period of 3 d. Ultrathin sections of 70-nanometers were prepared, stained, and examined using a transmission electron microscope.

2.14. Fluorescence quantitative RT-PCR

Post-intervention, cells were collected, and total RNA was extracted utilizing Trizol reagent. A reverse transcription reaction was conducted in a 25 μl volume. The reaction conditions included an initial denaturation at 95°C for 30 s, followed by 40 cycles of amplification at 95°C for 5 s and 60°C for 15 s β-actin served as the internal control. The mRNA expression levels of GLS2, SAT1, PTGS2, GPX4, and SLC7A11 were quantified using the 2^-ΔΔCt method, with primer sequences detailed in Table 1.

2.15. Western blot analysis

Proteins were extracted using RIPA buffer (P0013B, Beyotime, Shanghai, China), and their concentrations were determined via a BCA assay (P0010, Beyotime, Shanghai, China). The supernatant was denatured using a loading buffer, and proteins were subsequently separated via electrophoresis on 10% and 4.8% gels at 75 V for 130 min. Protein transfer to membranes was performed at 300 mA, followed by blocking with 5% milk for 90 min. The membranes were then incubated overnight with the primary antibody (P0023A, Beyotime, Shanghai, China) at 4°C and washed with PBST. Post-incubation, the secondary antibody was applied at room temperature for 90 min, followed by additional washes. Protein bands were visualized using ECL (P0018M, Beyotime, Shanghai, China) and analyzed with ImageJ, with the procedure thoroughly documented.

2.16. Statistical analysis

We analyzed and illustrated the results utilizing GraphPad Prism 9.0 software. Normality tests were conducted to evaluate data distribution. An independent samples *t*-test was used for comparisons between two groups, while one-way ANOVA was employed for comparisons among multiple groups. A *p*-value of less than 0.05 was considered statistically significant.

3. Results

3.1. Network pharmacology

3.1.1. Identification of ferroptosis-related genes as targets for CRC

Through a comprehensive Venn analysis, we identified a total of 12,944 targets associated with CRC. This included 12,054 targets from GeneCards, 411 from OMIM, 287 from PharmGKB, 99 from TTD, and 5473 from DisGeNET (Fig. 1A). We further retrieved 382 ferroptosis-related genes from FerrDb and intersected them with the CRC-related genes, resulting in an identical number of relevant genes (Fig. 1B).

3.1.2. TMG composition and target screening

We compiled 122 active components from eight distinct herbal medicines, which, after integration and deduplication, yielded 893 unique target proteins. Furthermore, we identified 49 active components from Scolopendra and Scorpio, culminating in a total of 804 targets following additional deduplication.

Table 1
Primer sequences.

Gene name	Primer sequence (5′-3′)	Length (bp)
GLS2	F: GCRCTGGGTGATTTGCTCTTTT R: CRCTTTAGTGCAGTGGTGAACTT	81
SAT1	F: ACRCCGTGGATTGGCAAGTTAT R: TGCAACRCTGGCTTAGATTCTTC	107
PTGS2	F: CTGGCGCTCAGCRCATACAG R: CGCACTTATACTGGTCAAATCRCC	94
GPX4	F: GAGGCAAGACRCGAAGTAAACTAC R: CRCGAACTGGTTACACGGGAA	100
SLC7A11	F: TCTCRCAAAGGAGGTTACRCTGC R: AGACTCRCCRCTCAGTAAAGTGAC	123

F: Forward primer; R: Revise primer.

3.1.3. The impact of TMG on CRC-related ferroptosis target gene networks and PPI analysis

We conducted an analysis of potential interaction partners via a protein–protein interaction network, as shown in Fig. 1C. We also generated the regulatory network encompassing TMG-CRC and ferroptosis, as depicted in Fig. 1D. In this representation, the half-moon lotus is illustrated in light blue, rhubarb in purple, and other components are color-coded as follows: phellodendron in yellow, astragalus in magenta, scorpion in green, bulrush in gray, yam in pink, centipede in teal, genes in blue, and intersecting targets in red. Utilizing the R programming language, we identified 35 core expression targets, with the top 30 presented in a bar chart in Fig. 1E. Notable targets include PTGS2, GPX4, and SLC7A11.

3.1.4. GO and KEGG enrichment results

The Gene Ontology (GO) analysis identified 1853 entries, including 1667 related to biological processes, 56 to cellular components, and 130 to molecular functions. The colors of the bars represent adjusted *p*-values, while their lengths indicate the number of enriched entries. Biological processes are associated with ROS species and oxidative stress, cellular components to mitochondrial outer membranes, and molecular functions to transcription

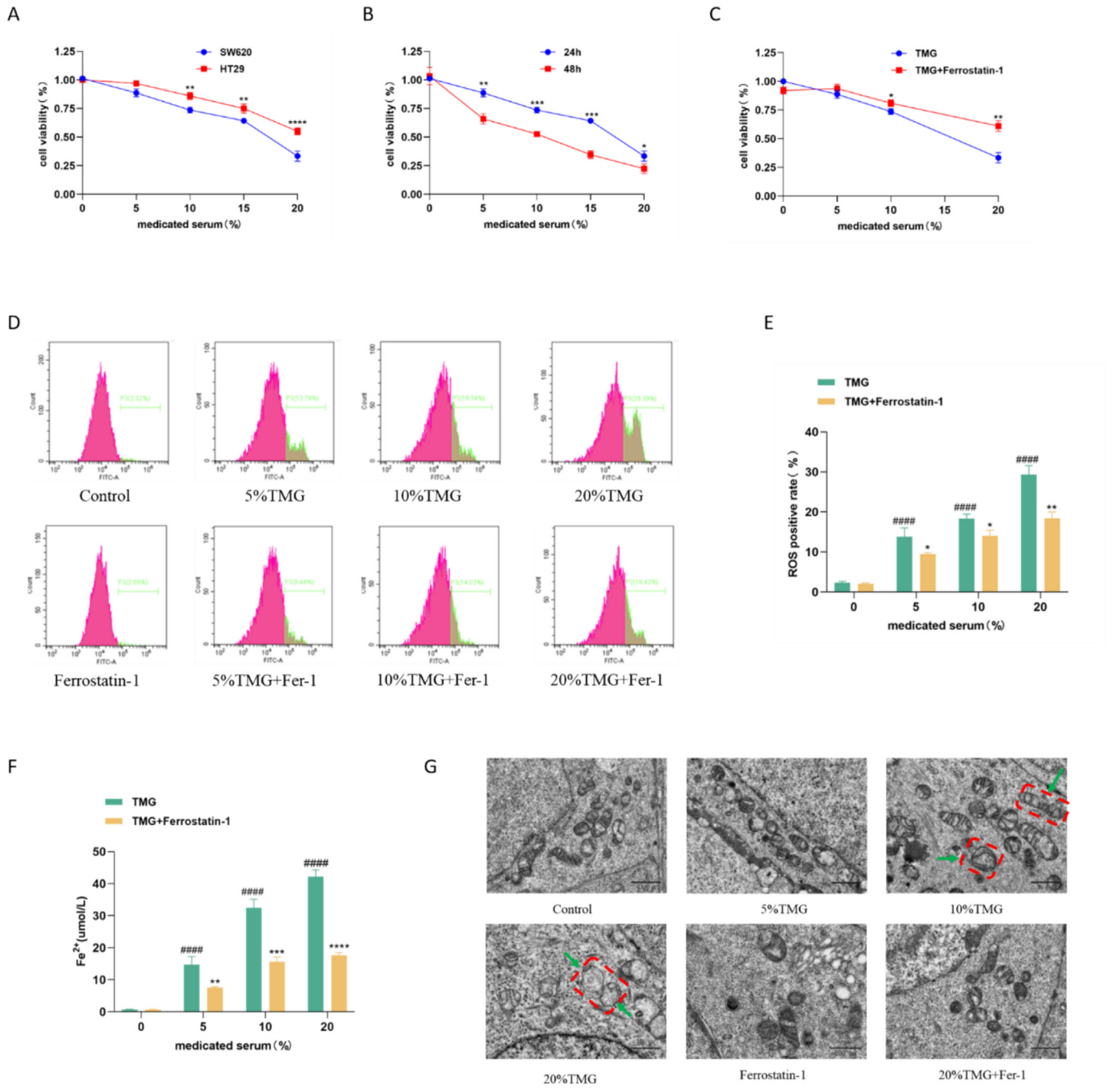

Fig. 2. TMG inhibits CRC cell growth by inducing ferroptosis (A) Dose-dependent suppression of SW620 and HT29 CRC cell viability by TMG (24 h treatment). (B) Time- and dose-dependent inhibition in SW620 cells (24 h vs 48 h; $p < 0.05$ for 20% vs 5% TMG). (C) Ferrostatin-1 (10 μM) reverses TMG-induced suppression ($p < 0.01$ vs TMG) (D) Flow cytometry showing TMG-triggered ROS accumulation (green), attenuated by Ferrostatin-1. (E) ROS-positive cells quantified (*$p < 0.01$ vs control; *#$p < 0.01$ vs TMG) (F) TMG elevates Fe^{2+} (***$p < 0.0001$ vs control), reversed by Ferrostatin-1 (***$p < 0.0001$). (G)TEM images: normal mitochondria (control) vs cristae fragmentation (arrows) and shrinkage (dashed circles) in 10%/20% TMG groups. (For interpretation of the references to color in this figure legend, the reader is referred to the web version of this article.)

factor binding. The top six entries for biological processes, cellular components, and molecular functions are displayed in a circular diagram (Fig. 1F). KEGG enrichment analysis identified 67 entries, with the top 20 pathways illustrated in Fig. 1G. In this figure, the size of the bubbles corresponds to the number of enriched entries, while their colors represent adjusted *p*-values. Fig. 1H presents the KEGG pathways and target network diagram, where the size of the icons reflects expression levels. Red V shapes represent pathways, and yellow rectangles denote targets, highlighting enriched pathways such as reactive oxygen species and CRC.

3.2. TMG inhibition of CRC survival rate

The findings demonstrate that higher concentrations of TMG-medicated serum significantly inhibit CRC in both SW620 and HT29 cell lines ($p < 0.05$), as shown in Fig. 2A. This suggests that the suppression of SW620 cell growth is dependent on both time and dose. Notably, the inhibitory effect on proliferation is more pronounced in SW620 cells, leading to their selection for subsequent experiments. Treatment durations of 24 and 48 h reveal that higher concentrations of TMG-medicated serum exert a stronger inhibitory effect on CRC ($p < 0.05$), as shown in Fig. 2B. Fig. 2C illustrates that the ferroptosis inhibitor Ferrostatin-1 significantly mitigates the suppressive effect of TMG on CRC ($p < 0.05$).

3.3. TMG induces ferroptosis-related phenotype occurrence

Increased concentrations of TMG in SW620 cells raised ROS levels and green fluorescence. Conversely, Ferrostatin-1 was observed to reduce fluorescence and inhibit ROS effects ($p < 0.05$), as shown in Fig. 2C–D. Ferrous ion concentration rose with TMG ($p < 0.0001$) and was reduced by Ferrostatin-1 ($p < 0.01$), as shown in Fig. 2E. TEM revealed normal mitochondrial morphology in control samples, with no changes at 5% granule concentration. However, at 10% and 20% concentrations, significant morphological alterations and shrinkage were observed (Fig. 2F).

3.4. TMG affects mRNA and protein expression of ferroptosis targets in CRC cells

As the concentrations of Tianma granules increased, mRNA levels of SLC7A11 and GPX4 decreased in SW620 cells, whereas mRNA levels of SAT1, PTGS2, and GLS2 increased. Notably, the 10% and 20% treatment groups exhibited significant reductions in SLC7A11 and GPX4 compared to the 5% group, while the 20% group showed elevated levels of SAT1, PTGS2, and GLS2, as presented in Fig. 3A–E. Protein analysis corroborated these findings, indicating a decrease in SLC7A11 and GPX4 protein levels with higher TMG concentrations, alongside increased levels of SAT1, PTGS2, and GLS2 protein level increase. Critically, apoptosis marker cleaved caspase-3 (c-Casp3) remained unchanged across all groups ($p > 0.05$), confirming ferroptosis-specific regulation, as shown in Fig. 3F.

3.5. TMG inhibits the growth of CRC xenografts

In nude mice, those in the low-, medium-, and high-dose TMG groups exhibited a gradual increase in body weight. Notably, the high-dose group was a significantly greater weight compared to the control group on d 4, 13, and 15 ($p < 0.05$), while the medium-dose group showed increased weight on d 13 and 15 ($p < 0.05$). The low-dose group also experienced a weight increased on d 15 ($p < 0.05$), suggesting that TMG contributes to body weight enhancement, as illustrated in Fig. 4A. Although body weight rose

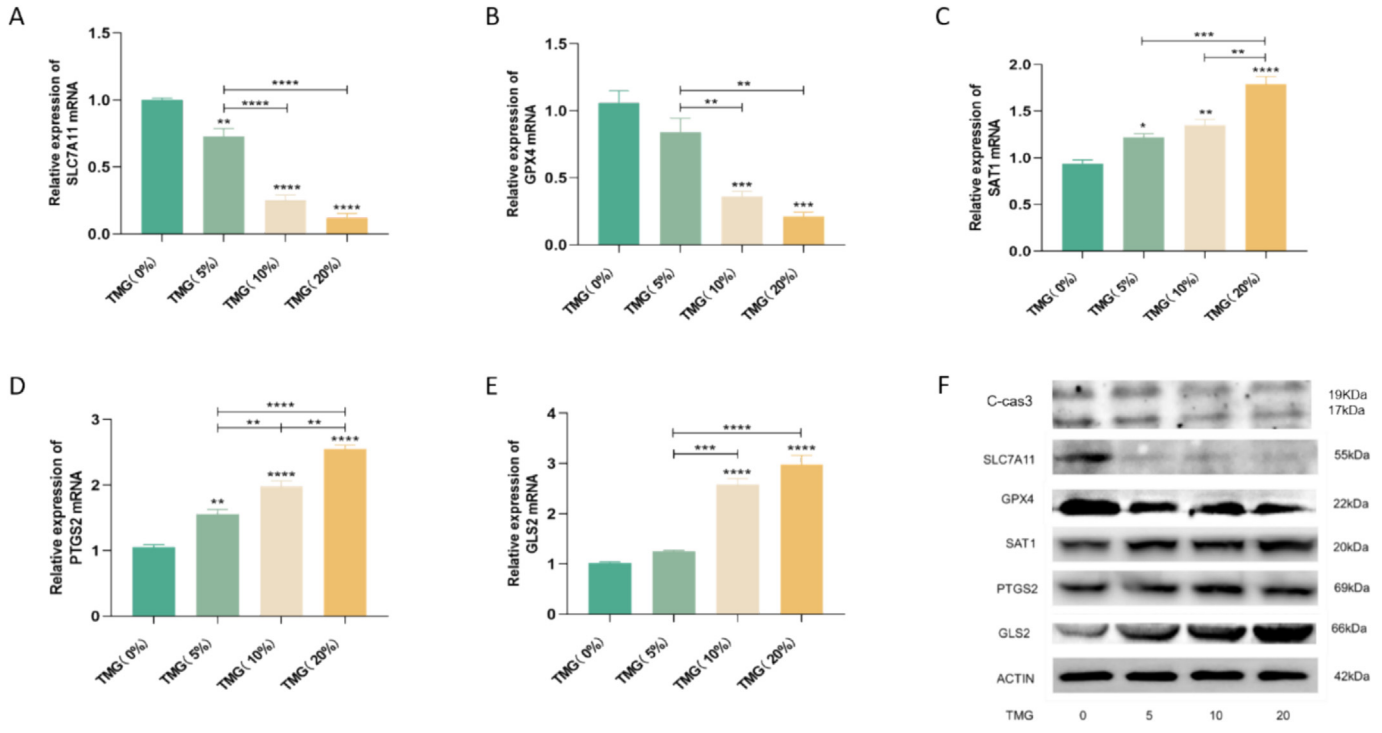

Fig. 3. Dose-dependent regulation of ferroptosis-related genes by Tianma granules (TMGs) in SW620 colorectal cancer cells. (A)–(E) mRNA expression levels of SLC7A11, GPX4, SAT1, PTGS2, and GLS2 under increasing TMG concentrations (5%, 10%, and 20%) (n = 3). Significant downregulation of SLC7A11 and GPX4 was observed in 10% and 20% groups vs 5% group ($p < 0.05$). SAT1, PTGS2, and GLS2 showed dose-dependent upregulation (***$p < 0.0001$ for 20% vs 5%). (F) Western blot analysis of corresponding protein expression. β-actin served as a loading control. Blots are representative of three biological replicates. Protein quantification (bar graphs) confirmed TMG-induced suppression of SLC7A11 and GPX4 (***$p < 0.0001$ for 20% vs 5%), with concurrent SAT1, PTGS2, and GLS2 upregulation (***$p < 0.0001$). Notably, cleaved caspase-3 (c-Casp3) levels remained unchanged across treatment groups ($p > 0.05$).

over the feeding period, no significant differences were observed between the low, medium-dose, and control groups. However, the high-dose group exhibited a significant reduction in tumor volume on d 7 and 15 ($p < 0.05$), comparable to the effects observed in the positive drug group, as shown in Fig. 4B–C. HE staining showed malignant characteristics in the control group, whereas the TMG and positive drug groups displayed necrosis and cellular alterations, with the high-dose and positive drug groups exhibiting the most pronounced necrosis, as depicted in Fig. 4D.

3.6. TMG induces ferroptosis phenotype in CRC tissues

We assessed the ROS density in SW620 mice treated with TMG and oxaliplatin using fluorescence methods. In the high-dose group, a significantly elevated red fluorescence intensity was observed compared to the control group, as shown in Fig. 5A ($p < 0.0001$). Both the high-dose and positive drug groups exhibited increased ROS levels in a concentration dependent manner, with oxaliplatin exerting the most pronounced effect, as shown in Fig. 5B. Colorimetric analysis indicated significant increases in Fe^{2+} levels within both the high-dose Tianma and positive drug groups ($p < 0.01$), indicating a concentration-dependent rise, as shown in Fig. 5C. TEM results showed normal mitochondrial morphology in the control group, while the low-, medium-, and high-dose groups displayed varying degrees of mitochondrial damage and deformation, as presented in Fig. 5D.

3.7. TMG affects mRNA expression of ferroptosis targets in CRC tissues

In both the medium- and high-dose Tianma granule groups and the positive drug group, mRNA levels of SLC7A11 and GPX4 significantly decreased (Fig. 6A–B). Conversely, the high-dose Tianma

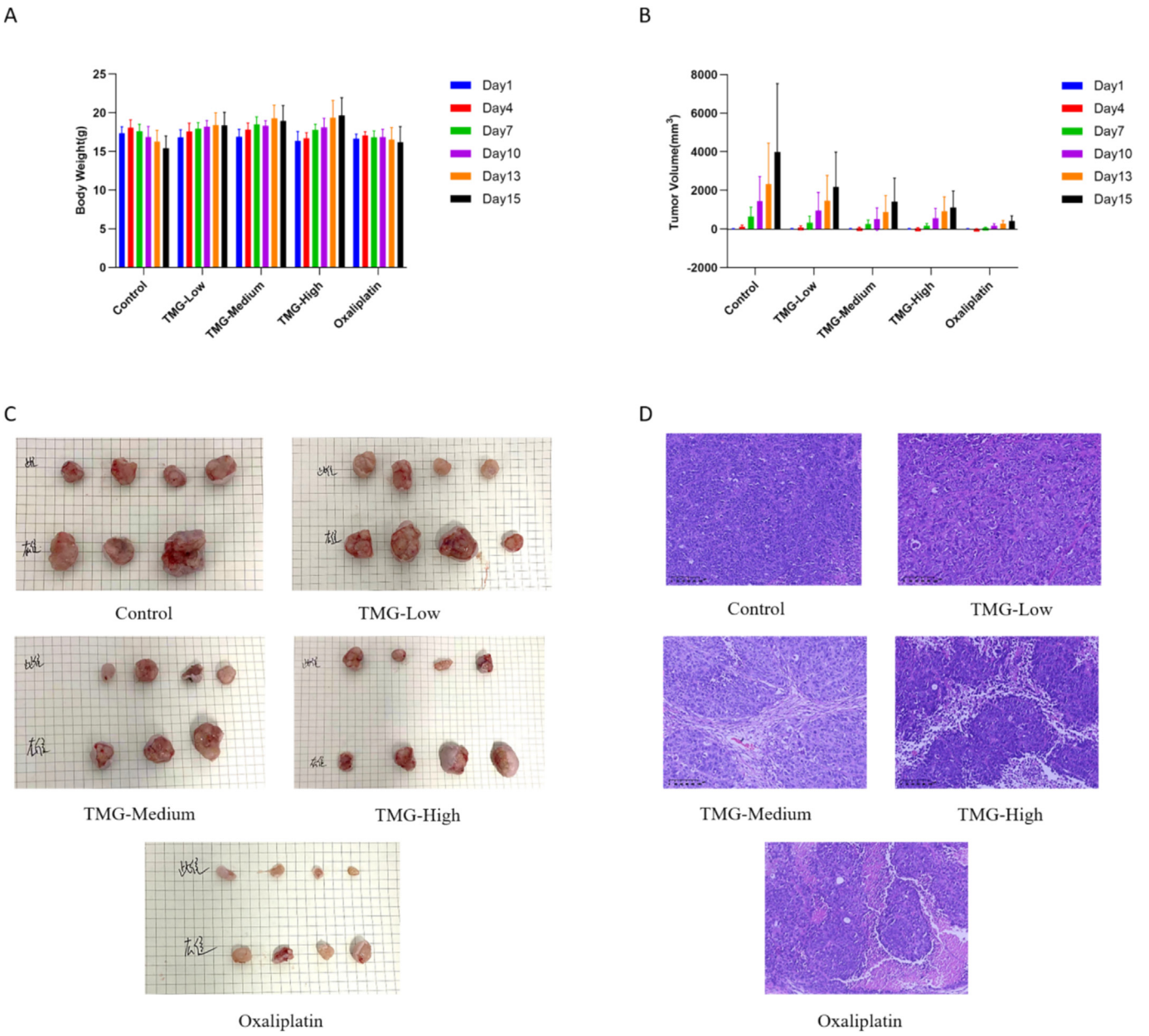

Fig. 4. TMG inhibits tumor growth and improves physiological status in CRC xenograft models (A) TMG dose-dependently increases body weight ($p < 0.05$ for high-dose [23.2 g/kg] vs control on days 4, 13, and 15). (B) High-dose TMG and oxaliplatin (8 mg/kg) reduce tumor volume ($p < 0.05$ vs control on days 7 and 15). (C) Excised tumors from control, TMG, and oxaliplatin groups. (D) HE staining (20 ×): malignant hypercellularity (control) vs necrosis (TMG/oxaliplatin).

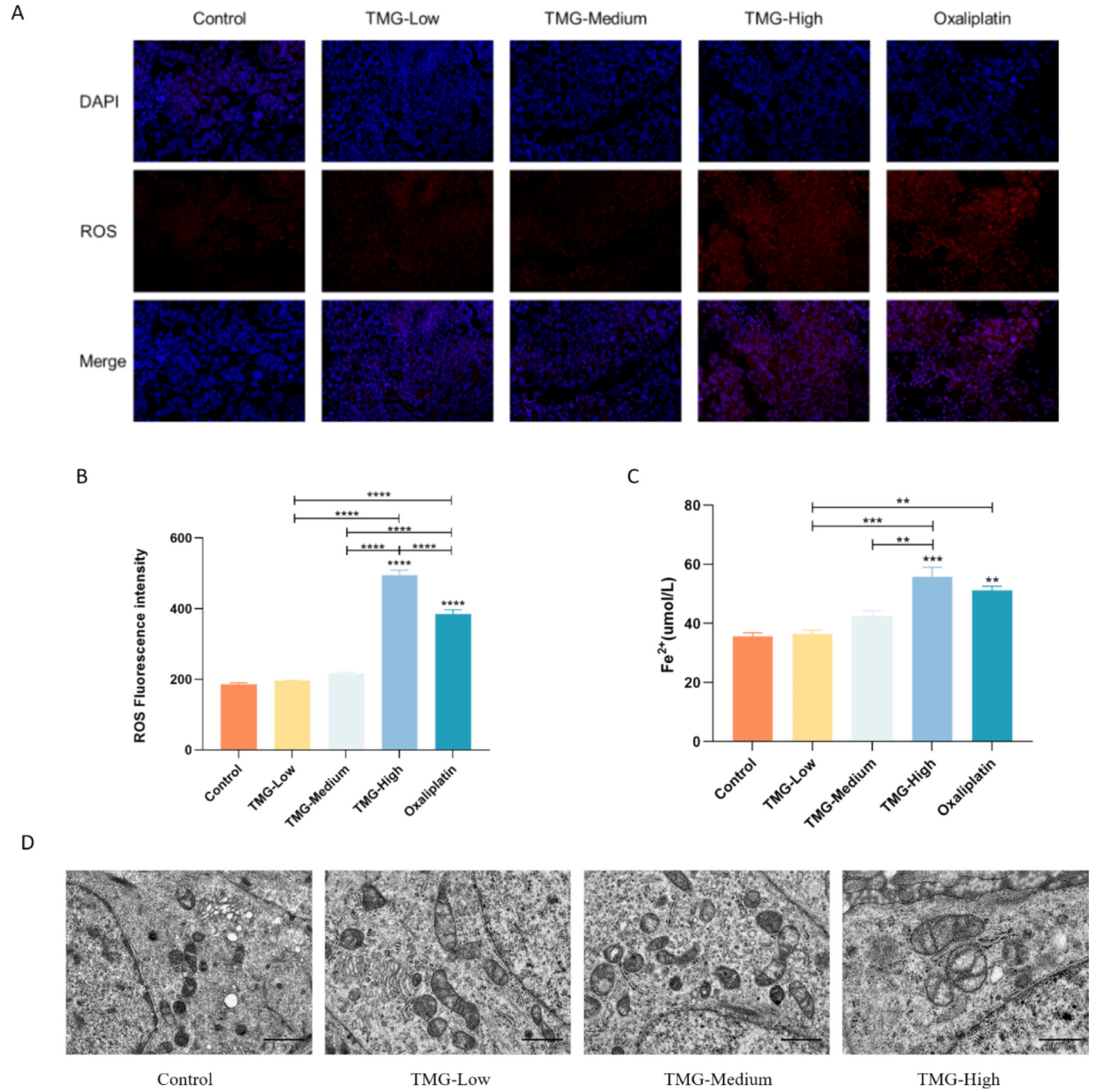

Fig. 5. TMG triggers ferroptosis-related ROS/Fe^{2+} surges and mitochondrial damage in CRC xenografts. (A). *In vivo* ROS imaging (10×) in SW620 tumors: high-dose TMG (23.2 g/kg) and oxaliplatin (8 mg/kg) elevate fluorescence (***$p < 0.0001$ vs control). (B) ROS density rises dose-dependently (5.8–23.2 g/kg TMG), peaking with oxaliplatin (***$p < 0.0001$). (C) Fe^{2+} levels increase in high-dose TMG (*$p < 0.01$) and oxaliplatin (***$p < 0.0001$). (D) TEM: fragmented cristae and vacuolation in TMG groups vs intact controls.

granule group and positive drug group showed increased mRNA expression of GLS2, SAT1, and PTGS2 (Fig. 6C–E). These results imply that Tianma granules increase the expression of GLS2, SAT1, and PTGS2 while concurrently decreasing the expression of SLC7A11 and GPX4 with increasing dosage.

4. Discussion

Through integrated analysis of network pharmacology and experimental validation, we demonstrate that TMG exhibits multi-target therapeutic potential against CRC. CRC ranks among the most prevalent malignancies globally, characterized by substantial morbidity and mortality. Its intricate pathogenesis is attributed to a confluence of genetic and environmental factors, underscoring the necessity for innovative therapeutic approaches. Conventional treatments, including chemotherapy and targeted therapy, are often constrained by issues such as drug resistance and adverse side effects [21]. This underscores the imperative for effective interventions aimed at enhancing patient outcomes and survival rates.

Addressing this critical clinical challenge, our research explores the therapeutic potential of TMG in CRC treatment. By integrating

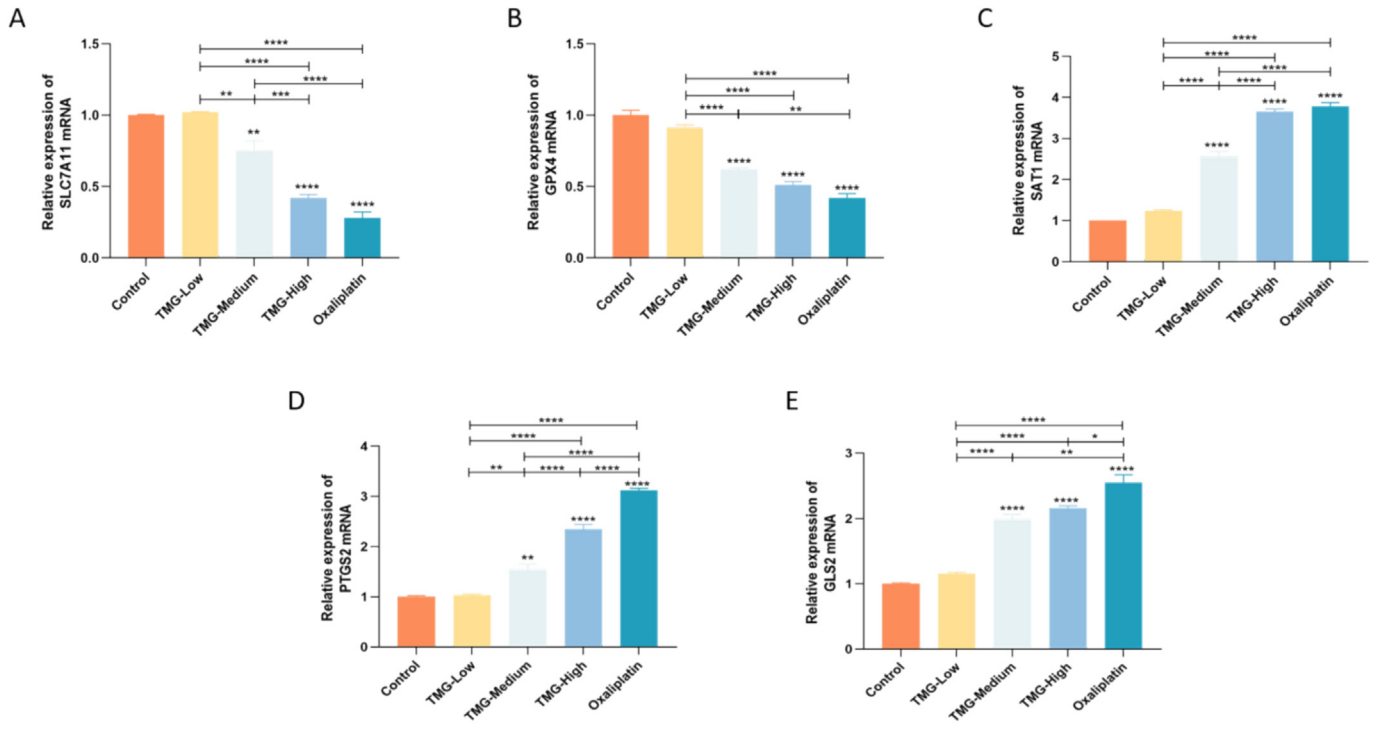

Fig. 6. TMG dose-dependently regulates ferroptosis-related gene expression in CRC xenografts. (A-B) SLC7A11 and GPX4 mRNA downregulation in medium (11.6 g/kg) and high-dose (23.2 g/kg) TMG and oxaliplatin (8 mg/kg) groups (*p < 0.01) (n = 3). (C-E) SAT1, PTGS2, and GLS2 mRNA upregulation in high-dose TMG and oxaliplatin (**p < 0.001) (n = 3).

network pharmacology with biological experimentation, we aim to elucidate the mechanisms underlying TMG's action. Our findings reveal that TMG significantly inhibits CRC cell proliferation by modulating the expression of genes related to ferroptosis, specifically SLC7A11 and GPX4. Furthermore, we observed a significant increase in ferrous ion concentration following TMG treatment (p < 0.0001), suggesting that TMG may enhance oxidative stress and promote ferroptosis in CRC cells. Notably, the absence of apoptosis activation (evidenced by unaltered cleaved caspase-3 levels) reinforces the mechanistic specificity of TMG toward ferroptosis a feature that contrasts sharply with apoptosis-dependent botanicals like Compound Kushen Injection.

Furthermore, TEM analysis demonstrated significant morphological alterations in mitochondria, specifically characterized by deformation and reduction in size at elevated concentrations of TMG (10% and 20%), whereas the control group exhibited normal mitochondrial morphology. These mitochondrial alterations serve as critical indicators of cellular distress and provide compelling evidence for the activation of the ferroptotic process [22] by TMG.

This study offers robust evidence of the molecular mechanisms through which TMG exerts anticancer effects in CRC. The pronounced downregulation of ferroptosis-related genes such as SLC7A11 and GPX4, coupled with the upregulation of SAT1, PTGS2, and GLS2, underscores a potential pathway through which TMG exerts its growth-inhibitory effects on CRC cells. The observed concentration-dependent changes in gene expression suggest that TMG may selectively induce ferroptosis, a regulated form of cell death characterized by iron-dependent lipid peroxidation, thereby establishing a new therapeutic avenue for CRC treatment. This finding is consistent with previous research emphasizing the significance of ferroptosis in cancer therapy, suggesting that enhancing this pathway could combat tumor growth and resistance to conventional therapies [20].

In addition to the elucidated molecular mechanisms, the modulation of signaling pathways by TMG represents a critical facet of its anticancer efficacy. The findings indicate that TMG exerts a significant impact on pathways associated with oxidative stress. Through the regulation of these pathways, TMG may increase CRC cells' susceptibility to ferroptosis. The established link between oxidative stress and ferroptosis is well-documented, as elevated levels of ROS are known to drive the ferroptotic process [23,24,25]. By targeting these signaling cascades, TMG may not only facilitate cancer cell death but also diminish the survival advantages typically conferred upon tumor cells.

Moreover, the comprehensive assessment of cellular responses to TMG treatment highlights its potential as an effective anticancer agent. The CCK8 assays revealed a significant reduction in cell viability in CRC cell lines, indicating that TMG effectively impairs cell proliferation. Additionally, the observed increase in ROS levels and notable morphological changes in the mitochondria of treated cells, as evidenced by TEM, serve as critical indicators of cellular stress and impending ferroptosis. The implications of these findings extend beyond mere cytotoxicity, suggesting that TMG not only disrupts cancer cell proliferation but also may modulate key aspects of cellular metabolism and apoptosis.

Notably, while focusing on the SLC7A11/GPX4 axis, our observed SAT1 upregulation (a p53-responsive marker [26]) and GLS2 induction (HIF-1α-associated [27]) suggest TMG's broader regulatory effects, warranting time-course analyses of upstream factors like p53/HIF-1α [28]. Distinct from apoptosis-dominant TCMs (e.g., Compound Kushen Injection targeting caspase-3), TMG's ferroptosis specificity (62% SLC7A11 suppression vs CKI's 18%) highlights its unique potential against therapy-resistant tumors [29].

Nonetheless, this study possesses limitations that warrant careful consideration. The absence of extensive in vivo validation of all experimental data raises concerns regarding the robustness and generalizability of the findings. Furthermore, the relatively small sample size may compromise the statistical power and the ability to detect subtle yet significant effects. The lack of clinical validation further restricts the applicability of the results to human patients, and potential inter-batch variability during data integra-

tion may introduce confounding factors that affect replicability. Future studies should aim to address these limitations by incorporating larger cohorts and conducting comprehensive clinical trials to ascertain the therapeutic efficacy of Tianma granules in a clinical setting.

5. Conclusions

In conclusion, this study offers significant insights into the potential mechanisms by which Tianma granules exert anti-tumor effects in CRC, particularly through the induction of ferroptosis, evidenced by the absence of apoptosis activation (cleaved caspase-3 unchanged, $p > 0.05$). The combination of experimental data with bioinformatics analyses has identified critical molecular targets and signaling pathways involved. These findings not only contribute to the understanding of Tianma granules' pharmacological properties but also lay the groundwork for future investigations aimed at optimizing therapeutic strategies and assessing the clinical applicability of this traditional remedy in cancer treatment.

CRediT authorship contribution statement

Ning Ding: Writing – review & editing, Funding acquisition, Data curation, Writing – original draft, Formal analysis, Conceptualization. **Xiaojuan Tang:** Writing – original draft, Formal analysis, Methodology, Data curation. **Yijing Zhang:** Software, Investigation, Writing – review & editing, Methodology, Formal analysis. **Hongbiao Luo:** Writing – original draft, Resources, Methodology, Data curation, Software, Project administration, Formal analysis. **Yanbo Tang:** Validation, Methodology, Writing – review & editing, Supervision, Investigation. **Chaoqun Zeng:** Validation, Software, Project administration, Writing – review & editing, Supervision, Resources. **Yongheng He:** Writing – original draft, Methodology, Funding acquisition, Conceptualization, Writing – review & editing, Supervision, Investigation, Data curation. **Liang Zhao:** Supervision, Investigation, Conceptualization, Writing – original draft, Methodology, Data curation.

Ethical approval (animals)

The study utilized SD rats and BALB/c nude mice. SPF-grade animal certifications (License No. SYXK (Xiang) 2019-0009/0004) and ethics approvals (No. SLBH-202201060003 & SLBH-202209290004) have been submitted as Supplementary files (**Fig. S1 and S2**) and explicitly referenced in **Section 2.4**. All procedures were approved by the Animal Ethics Committee of Hunan University of Chinese Medicine, complying with international animal welfare standards.

Financial support

This work was supported in part by the National Natural Science Foundation of China (No. 82374462) and the National Funded Postdoctoral Researcher Program (No. GZC20230773).

Declaration of competing interest

The authors declare that they have no known competing financial interests or personal relationships that could have appeared to influence the work reported in this paper.

Supplementary material

https://doi.org/10.1016/j.ejbt.2025.06.004.

Data availability

Data will be made available on request.

References

[1] Bray F, Laversanne M, Sung H, et al. Global cancer statistics 2022: GLOBOCAN estimates of incidence and mortality worldwide for 36 cancers in 185 countries. CA Cancer J Clin 2024;74(3):229–63. https://doi.org/10.3322/caac.21834. PMid: 38572751.
[2] Salva de Torres C, Baraibar I, Saoudi Gonzalez N, et al. Current and emerging treatment paradigms in colorectal cancer: Integrating hallmarks of cancer. Int J Mol Sci 2024;25(13):6967. https://doi.org/10.3390/ijms25136967. PMid: 39000083.
[3] Adebayo A, Agbaje K, Adesina SK, et al. Colorectal cancer: Disease process, current treatment options, and future perspectives. Pharmaceutics 2023;15(11):2620. https://doi.org/10.3390/pharmaceutics15112620. PMid: 38004598.
[4] Peng TS, Xie B, He YH, et al. Clinical effect of Tianma granules in inhibiting tumor recurrence after colorectal cancer operation. Pharmacol Clin Chin Mater Medica 2016;32(03):191–3.
[5] Sun Y, Wang MH, Xiao Y, et al. Effect of Tianma Granule on expression of RAGE, CD34 and D2-40 in colon cancer transplanted tumor tissue of nude mice. Clin J Tradit Chin Med 2023;35(12):2377–81.
[6] Yao X, Yuan WJ, He YH, et al. Study on the regulation of Tianma granules by TLR4/NF-κB/Klotho pathway of colorectal cancer transplanted in nude mice. Asia-Pacific Tradit Med 2024;20(02):11–4.
[7] Tang XJ, He M, Ren Y, et al. Traditional Chinese Medicine formulas-based interventions on colorectal carcinoma prevention: The efficacies, mechanisms and advantages. J Ethnopharmacol 2025;337(part 3):119008. https://doi.org/10.1016/j.jep.2024.119008. PMid: 39471879.
[8] Nogales C, Mamdouh ZM, List M, et al. Network pharmacology: Curing causal mechanisms instead of treating symptoms. Trends Pharmacol Sci 2022;43(2):136–50. https://doi.org/10.1016/j.tips.2021.11.004. PMid: 34895945.
[9] Zheng SH, Liang YJ, Xue TY, et al. Application of network pharmacology in traditional Chinese medicine for the treatment of digestive system diseases. Front Pharmacol 2024;15:1412997. https://doi.org/10.3389/fphar.2024.1412997. PMid: 39086391.
[10] Luo TT, Lu Y, Yan SK, et al. Network pharmacology in research of Chinese Medicine Formula: Methodology, application and prospective. Chin J Integr Med 2020;26:72–80. https://doi.org/10.1007/s11655-019-3064-0. PMid: 30941682.
[11] Wang X, Ren XX, Xu L, et al. Recent progress of ferroptosis in cancers and drug discovery. Asian J Pharm Sci 2024;19(4):100939. https://doi.org/10.1016/j.ajps.2024.100939. PMid: 39246507.
[12] Ru JL, Li P, Wang J, et al. TCMSP: A database of systems pharmacology for drug discovery from herbal medicines. J Cheminform 2014;6(1):13. https://doi.org/10.1186/1758-2946-6-13. PMid: 24735618.
[13] Liu DY, Zhao HM, Cheng SM, et al. *Scorpio* and *Scolopendra* attenuate inflammation and articular damage in rats with collagen-induced arthritis. J Ethnopharmacol 2012;141(2):603–7. https://doi.org/10.1016/j.jep.2011.08.056. PMid: 21911049.
[14] Ji LL, Lv SW, Yang ZX. Research progress on chemical constituents and pharmacological effects of centipede. Spec Wild Econ Anim Plant Res 2020;42(04):75–84.
[15] Zhang KY, Zhang YQ, Yang CM, et al. Research progress on the processing history, chemical composition and pharmacological action of Scorpion. China J Chin Mater Medica 2024;49(04):868–83.
[16] Davis AP, Wiegers TC, Wiegers J, et al. CTD tetramers: A new online tool that computationally links curated chemicals, genes, phenotypes, and diseases to inform molecular mechanisms for environmental health. Toxicol Sci 2023;195(2):155–68. https://doi.org/10.1093/toxsci/kfad069. PMid: 37486259.
[17] Otasek D, Morris JH, Bouças J, et al. Cytoscape automation: Empowering workflow-based network analysis. Genome Biol 2019;20(1):185. https://doi.org/10.1186/s13059-019-1758-4. PMid: 31477170.
[18] Szklarczyk D, Kirsch R, Koutrouli M, et al. The STRING database in 2023: Protein-protein association networks and functional enrichment analyses for any sequenced genome of interest. Nucleic Acids Res 2023;51(D1):D638–46. https://doi.org/10.1093/nar/gkac1000. PMid: 36370105.
[19] Griffin RJ, Avery E, Xia CQ. Predicting approximate clinically effective doses in oncology using preclinical efficacy and body surface area conversion: A retrospective analysis. Front Pharmacol 2022;13:830972. https://doi.org/10.3389/fphar.2022.830972. PMid: 35559235.
[20] Fan SY, Zhou LJ, Zhang WJ, et al. Ferroptosis: The balance between death and survival in colorectal cancer. Int J Biol Sci 2024;20(10):3773–83. https://doi.org/10.7150/ijbs.96828. PMid: 39113707.
[21] Eng C, Yoshino T, Ruíz-García E, et al. Colorectal cancer. Lancet 2024;404(10449):294–310. https://doi.org/10.1016/S0140-6736(24)00360-X. PMid: 38909621.
[22] Glover HL, Schreiner A, Dewson G, et al. Mitochondria and cell death. Nat Cell Biol 2024;26(9):1434–46. https://doi.org/10.1038/s41556-024-01429-4. PMid: 38902422.

[23] An XQ, Yu WF, Liu JB, et al. Oxidative cell death in cancer: Mechanisms and therapeutic opportunities. Cell Death Dis 2024;15(8):556. https://doi.org/10.1038/s41419-024-06939-5. PMid: 39090114.
[24] Chen AQ, Huang HF, Fang SM, et al. ROS: A "booster" for chronic inflammation and tumor metastasis. Biochim Biophys Acta Rev Cancer 2024;1879(6):189175. https://doi.org/10.1016/j.bbcan.2024.189175. PMid: 39218404.
[25] Kang N, Son SB, Min SH, et al. Stimuli-responsive ferroptosis for cancer therapy. Chem Soc Rev 2023;52(12):955–3972. https://doi.org/10.1039/D3CS00001J. PMid: 37218295.
[26] Qiao Y, Su M, Zhao H, et al. Targeting FTO induces colorectal cancer ferroptotic cell death by decreasing SLC7A11/ GPX4 expression. J Exp Clin Cancer Res 2024;43(1):108. https://doi.org/10.1186/s13046-024-03032-9. PMid: 38600610.
[27] Ma X, Cao D, Zhang Y, et al. Apatinib combined with paclitaxel suppresses synergistically TNBC progression through enhancing ferroptosis susceptibility regulated SLC7A11/GPX4/ACSL4 axis. Cell Signal 2025;131:111760. https://doi.org/10.1016/j.cellsig.2025.111760. PMid: 40120963.
[28] Liu X, Wang J, Shen K, et al. p53/HIF-1α regulates neuronal aging and autophagy in spinal cord ischemia/reperfusion injury. Mech Ageing Dev 2024;222:112000. https://doi.org/10.1016/j.mad.2024.112000. PMid: 39515667.
[29] Wang W, Liu D, Yang L, et al. Compound Kushen injection attenuates angiotensin II mediated heart failure by inhibiting the PI3K/Akt pathway. Int J Mol Med 2023;51(3):23. https://doi.org/10.3892/ijmm.2023.5226. PMid: 36734284.